Wakefield benchmarking at a single-pass high brightness electron linac

S. Di Mitri,[1,2,*] C. Venier,[2] R. Vescovo,[2] and L. Sturari[1]
[1]*Elettra—Sincrotrone Trieste S.C.p.A., 34149 Basovizza, Trieste, Italy*
[2]*University of Trieste, Department of Engineering and Architecture, Via A. Valerio 6/1, 34127 Trieste, Italy*

(Received 7 November 2018; published 4 January 2019)

Collective effects such as wakefields affect the dynamics of high brightness electron beams in linear accelerators (linacs) and can degrade the performance of short wavelength free-electron lasers (FELs). If a reliable model of wakefields is made available, the accelerator can be designed and configured with parameters that minimize their disrupting effect. In this paper, the simulated effect of geometric (diffractive) wakefields and of coherent synchrotron radiation on the electron beam energy distribution at the FERMI FEL is benchmarked with measurements, so quantifying the accuracy of the model. Wakefield modeling is then extended to the undulator line, where particle tracking confirms the limited impact of the resistive wall wakefield on the lasing process. The study reveals an overall good understanding of collective effects in the facility.

DOI: 10.1103/PhysRevAccelBeams.22.014401

I. INTRODUCTION

The advent of subpicosecond-long electron bunches with hundreds of ampere peak current and submicron-level energy-normalized transverse emittances, such as those driving linac-based extreme ultraviolet and x-ray free electron lasers (FELs) [1–7], has raised the awareness of the accelerator community to the dilution of the electron beam brightness (i.e., six-dimensional charge density) by the interaction with wakefields in the accelerator and with coherent synchrotron radiation (CSR) in magnetic compressors [8]. If an accurate modeling of wakefields is made available, their disrupting effect on the beam quality, and therefore on the FEL performance, can be simulated and thereby minimized with a suitable choice of linac and beam parameters (e.g., rf phases, trajectory bumps, bunch charge, bunch length, etc.) [9].

At the FERMI FEL [6,7], a systematic study of collective effects has been carried out since the early stage of machine design [10–14]. Figure 1 sketches the current facility layout. In the past decade, numerical predictions were benchmarked with experimental results to demonstrate the interplay of longitudinal geometric wakefields and the beam current profile [15,16], to quantify the effect of transverse wakefields on the beam projected emittance [9,17], and to compare one- vs three-dimensional CSR effects on the beam emittance [18–20]. They all confirm, on top of the routine operation of the facility, that the electron beam dynamics is strongly affected by geometric (diffractive) wakefields in the linac sections ($L0$–$L4$ in Fig. 1) and by CSR emission in the magnetic chicane devoted to bunch length compression (BC1). In addition to this, a semianalytical formulation of the resistive wall wakefield in the undulator elliptical vacuum chamber was provided [21]. Still, a systematic characterization of the longitudinal wakefields acting in the linac, as well as a start-to-end particle tracking run in the presence of a resistive wall wakefield in the undulator line, is lacking. The present work targets these two points.

After a theoretical introduction to wakefields (Sec. II), we complement the aforementioned studies by investigating (Sec. III A) the effect of linac geometric wakefields and of CSR on the beam energy distribution. The effect is quantified by measuring the beam mean energy and energy spread in a spectrometer line installed at the linac end, as a function of the bunch length and bunch charge. The final bunch length is determined by magnetic compression in BC1, and it was varied by scanning the rf phase of $L1$ (see Fig. 1). The bunch charge was varied by changing the intensity of the laser pulse that drives the photoelectron emission at the gun cathode. The study is extended (Sec. III B) to the computation and simulation of resistive wall wakefields in the FERMI FEL-2 undulator vacuum chamber. This is the second and longer undulator line of the two currently installed at FERMI. It is devoted to the emission of the shortest FEL wavelengths, in the range 4–20 nm, and it is expected to be more sensitive to the degradation of electron beam brightness. We reach conclusions in Sec. IV.

*Present address: Department of Physics, Via A. Valerio 2, 34127 Trieste, Italy.

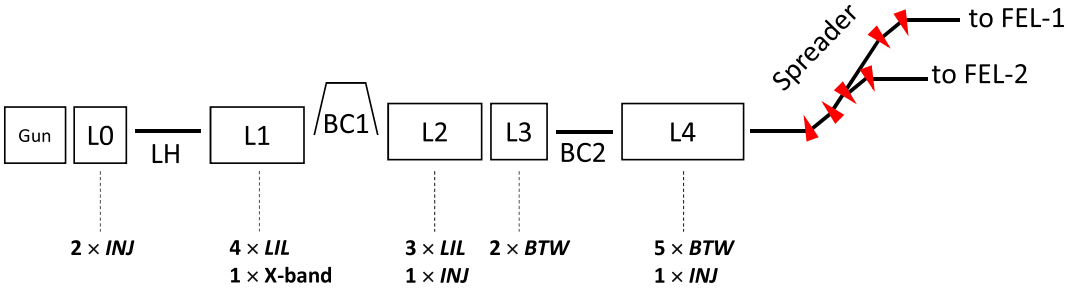

FIG. 1. Sketch (not to scale) of the FERMI electron beam delivery system. The electron beam is generated in the rf gun by photoelectron emission from a copper cathode illuminated by a UV laser. Electrons are accelerated up to 1.5 GeV in the *L*0–*L*4 *S*-band linac sections. It is time compressed, nominally by a factor of ∼10, in the BC1 bunch compressor, at the energy of 0.3 GeV (BC2 is not used routinely). Each linac section includes different traveling wave accelerating structures, which are grouped by length and inner geometry. They are of type "INJ" (3.2 m long each; 9 mm average radius), "LIL" (4.5 m long each; 10 mm average radius), "BTW" (6.1 m long each; 5 mm average radius), and "*X* band" (0.75 m long; 5 mm average radius). "LH" stays for laser heater. The whole linac is 175 m long. The spreader transfer line is ∼30 m long. The FEL-1 and FEL-2 undulator lines are, respectively, 30 and 44 m long.

II. WAKEFIELD MODEL

A. Wake function and wake potential

The longitudinal (transverse) wake function $G(s)$, measured in V/C [V/(Cm)], is defined as the path integral of the electromagnetic (e.m.) field excited by a point charge q and evaluated at a distance s behind it. The convolution of the wake function with the bunch charge distribution $\lambda(z)$, integrated along the beam path and normalized to the total bunch charge Q, is called the wake potential [22]. This is commonly expressed in V/C (longitudinal) or V/(Cm) (transverse) and is a measure of the e.m. fields generated by a bunch of ultrarelativistic charged particles in correspondence of, for example, variation of the vacuum vessel cross section (geometric or diffractive wakefield) [23], finite conductivity of the metallic vacuum vessel (resistive wall wakefield) [23], or emission of CSR in dipole magnets [24]. In the literature, the geometric wake function and wake potential of periodic rf structures are often evaluated per unit length, thus expressed in units of V/(Cm) and V/(Cm^2) for the longitudinal and transverse wakefield, respectively.

While the first two types of wakefield obey the causality principle, so that the field generated by leading particles in the bunch affects only trailing particles (head-to-tail interaction), the CSR effect, in the absence of shielding, is in fact a tail-to-head interaction [25]. The Fourier transform of the wake potential normalized to the Fourier transform of the bunch charge distribution function is called the impedance. In the following, only longitudinal wakefields are considered, i.e., e.m. fields modifying the particle longitudinal momentum. Moreover, we are interested in short-range wakefields, namely, wakefields interacting with their own bunch source: In FERMI, consecutive bunches are separated by 2 or 10 ms, and the amplitude of long-range wakefields becomes negligible over that time interval [12]. The single particle energy variation induced by the longitudinal wakefield is

$$\Delta E(z) = -eQ \int_{-\infty}^{z} \lambda(z') G_l(z - z') dz', \tag{1}$$

where the line-charge distribution $\lambda(z)$ is normalized to unity, so that $\frac{1}{Q}\int_{-\infty}^{\infty}\int_{-\infty}^{\infty}\int_{-\infty}^{\infty}\rho(x,y,z)dxdydz \equiv \int_{-\infty}^{\infty}\lambda(z)dz = 1$, and where ρ is the volume-charge density. Equation (1) assumes no dependence of the longitudinal wake function on the particle transverse coordinates (dipole field approximation). This is a realistic picture in the case of transverse beam sizes much smaller than the rf structure or vacuum chamber inner radius and for a beam well aligned on the element's longitudinal axis. These approximations are typically well satisfied in FERMI and will be used throughout the rest of this article. The average beam energy loss and the beam rms energy spread induced by the wakefield are, respectively,

$$\begin{aligned} \langle \Delta E \rangle &= \int_{-\infty}^{+\infty} \lambda(z') \Delta E(z') dz', \\ \sigma_E^2 &= \int_{-\infty}^{+\infty} \lambda(z') [\Delta E(z') - \langle \Delta E \rangle]^2 dz'. \end{aligned} \tag{2}$$

B. Geometric wakefield in rf structures

The excitation of a geometric wakefield is due to discontinuities of the vacuum vessel, and therefore the wakefield is expected to be related to the vessel geometry. The longitudinal geometric wake functions *per unit length* associated to the diverse inner geometries of the FERMI *S*-band accelerating structures match qualitatively the so-called Bane's model for disk-loaded rf structures, according to which the generic expression of the wake function and of the corresponding impedance (in the limit of high frequencies) per unit length is [26]

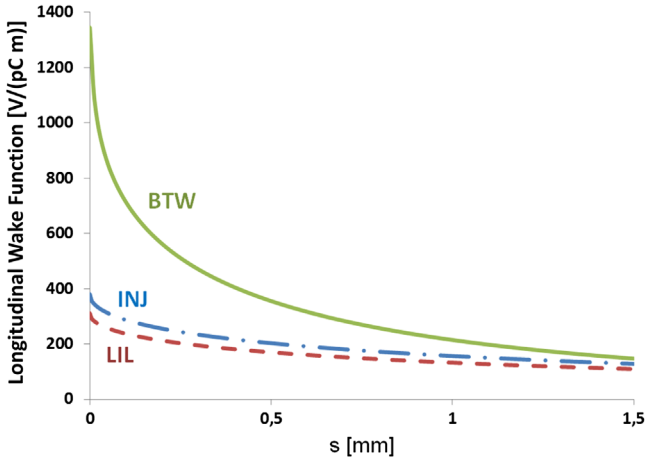

FIG. 2. Geometric longitudinal wake functions per unit length associated to the diverse inner geometries of the FERMI S-band accelerating structures; see Eq. (4). Labels refer to the structure naming adopted in Fig. 1. The value of the BTW wake function at $s = 0$ is defined according to the fundamental theorem of beam loading [23].

$$G_l(s) \propto \frac{Z_0 c}{\pi a^2} e^{-\sqrt{s/s_0}}, \qquad Z_l(k) \approx \frac{iZ_0}{\pi k a^2}. \tag{3}$$

In Eq. (3), we introduced $Z_0 = 120\pi\,\Omega$ for the vacuum impedance, c the light speed in vacuum, a the structure inner iris radius, and s_0 a parameter related to the cell geometry, typically in the range 1–3 mm for S-band linacs. Bane's model is valid for bunch lengths in the range $\frac{a^2}{2L} \ll \sigma_z \ll s_0$, with L the total structure length. This condition is satisfied in the FERMI linac, where $a \sim 5$–10 mm, $L \sim 3$–6 m, and $\sigma_z \sim 80$–800 μm.

The analytical expressions of the FERMI linac wake functions, in units of $\mathrm{V}/(\mathrm{pC\,m})$, are given in Eq. (4) and are plotted in Fig. 2. They well represent the e.m. field pattern established along the whole multicell accelerating structure and apply to bunch lengths shorter than 5 mm [10,12]. The uppercase label of each wake function refers to the structure naming in Fig. 1. Please note that the numerical coefficients are consistent with the s coordinate expressed in units of meters.

$$w_l^{\mathrm{INJ}}(s) = 380 \cdot e^{-\sqrt{s/(1.28\times10^{-3})}}, \tag{4a}$$

$$w_l^{\mathrm{LIL}}(s) = 311 \cdot e^{-\sqrt{s/(1.38\times10^{-3})}}, \tag{4b}$$

$$w_l^{\mathrm{BTW}}(s) = 1226 \cdot e^{-\sqrt{s/(3\times10^{-4})}} + \frac{0.494}{\sqrt{s}} + 494 \cdot \sqrt{s}. \tag{4c}$$

C. Resistive wall wakefield in cylindrical and parallel plate chamber

The excitation of a resistive wall wakefield is due to the finite conductivity of the metallic beam pipe. The conductivity depends on the frequency of the e.m. field applied, which is inversely proportional to the length of the source bunch. According to the Drude-Sommerfeld model [27], the ac conductivity evaluated at the wave number k is $\sigma_{ac}(k) = \frac{\sigma_{dc}}{1-ikc\tau}$, where $\sigma_{dc} = \frac{Qe\tau}{m_e}$ and τ is the characteristic relaxing time of the beam pipe material. Since we are interested in short-range wakefields generated by short bunches, i.e., producing e.m. field at high frequencies, we will simulate the ac component only of the resistive wall wakefield.

The FERMI undulator vacuum chamber is made of 1.1-m-long sections in stainless steel (INOX) 304LN, of cylindrical cross section and 11 mm inner radius. These are interleaved by 3.2-m-long elliptical chambers in aluminum, of inner diameters 7 mm × 22 mm. Since the ellipticity of the elliptical chambers is larger than 3, the wake function can be approximated to that of parallel plates at a gap equal to the shortest (vertical) diameter [21].

The longitudinal resistive wall impedance of a cylindrical metallic vacuum chamber of inner radius b and conductivity σ_{ac} is [23]

$$Z_{ac}^{\mathrm{cyl}}(k) = \frac{Z_0}{2\pi b}\left(\frac{f(k)}{k} - i\frac{kb}{2}\right)^{-1}. \tag{5}$$

The wake function is calculated as the inverse-Fourier transform of Eq. (5):

$$G_{l,ac}(z) = \frac{2c}{\pi}\int_0^\infty \mathrm{Re}[Z_{ac}(k)]\cos(kz)dk. \tag{6}$$

The analytical expression of the longitudinal resistive wall impedance of parallel plates is known from the Bane and Stupakov model in the limit $s_1 \ll b$, where $s_1 = \sqrt[3]{\frac{2b^2}{Z_0\sigma_{dc}}}$ estimates the distance at which the wakefield associated to σ_{ac} in a cylindrical pipe of inner radius b is damped [28,29]. That condition is satisfied at FERMI, and the wake function is calculated as the inverse-Fourier transform of the following impedance:

$$Z_{ac}^{pp}(k) = \frac{Z_0}{4\pi}\int_{-\infty}^{+\infty}\left(\frac{f(k)}{k}[\cosh(bx)]^2 - i\frac{k}{x}\cosh(bx)\sinh(bx)\right)^{-1}dx. \tag{7}$$

Figure 3 compares the single bunch energy variation per unit length [see Eq. (2)] induced by the dc and the ac resistive wall impedance in a cylindrical stainless steel vacuum chamber of inner radius 11 mm. Figure 4 compares the energy variation induced by the ac and dc impedance of a 7-mm-large gap aluminum parallel plate chamber with that one induced in a cylindrical chamber. The longitudinal

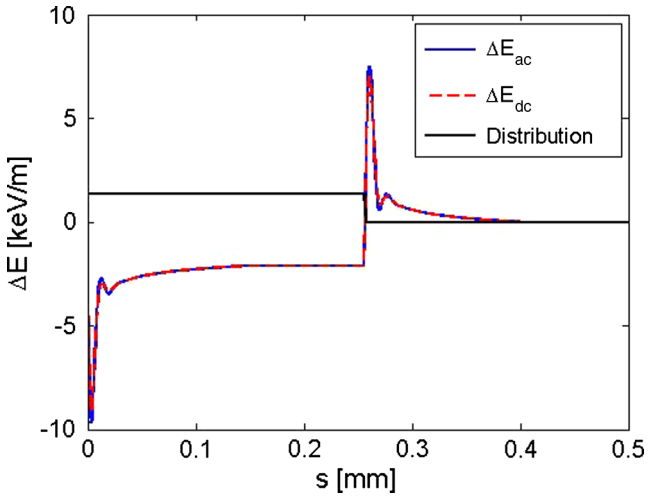

FIG. 3. Single bunch energy variation induced by ac (solid line) and dc (dashed line) resistive wall impedance excited by a 0.7 nC, 0.8-ps-long uniform charge distribution (black line) in a cylindrical vacuum chamber made of stainless steel 304LN and with 11 mm inner radius.

charge distribution is assumed to be uniform, since this resembles the typical current profile measured at FERMI, and the bunch charge is at the nominal value of 0.7 nC.

D. Coherent synchrotron radiation

A CSR tail-head interaction happens when synchrotron radiation emitted by trailing particles in the bunch catches up with leading particles by virtue of the curved electrons path in a dipole magnet. The variation induced in the particle longitudinal momentum is dominated by synchrotron radiation emitted coherently, i.e., at wavelengths comparable to or longer than the bunch length. At such wavelengths, typically corresponding to the terahertz frequency range, the characteristic angular divergence of synchrotron radiation becomes weakly dependent on the particle energy and is large enough to be comparable to the dipole bending angle [30], thus to allow photons emitted by the bunch tail to catch up with the head inside the same dipole. When the transverse dependence of the CSR electric field on the particle transverse coordinates is neglected (1D approximation), its longitudinal component at the interaction point reduces to [31]

$$E_{\parallel} = \frac{e}{24^{1/3}\pi\epsilon_0 R^{2/3}} \left\{ \frac{[\lambda(z-s_L)-\lambda(z-4s_L)]}{s_L^{1/3}} + \int_{z-s_L}^{z} \frac{d\lambda(z')}{dz'} \frac{dz'}{(z-z')^{1/3}} \right\}, \tag{8}$$

where R is the dipole curvature radius and we introduced the electron-photon path-length difference over a curved path, $s_L = R\theta - 2R\sin(\theta/2) \cong \frac{R\theta}{2\gamma^2} + \frac{R\theta^3}{24}$, and θ is the bending angle; for beam energies of interest here, the term $1/\gamma^2$ can be neglected. Equation (8) is implemented in the ELEGANT code [32,33]. The term in square brackets in Eq. (8) plays a role at the entrance of the dipole magnet ("entrance transient" effect). The integral dominates as the bending angle becomes large ("steady-state" emission), i.e., $\theta \geq (24\sigma_z/R)^{1/3}$ [31]. Propagation of the CSR field through a drift section immediately following the dipole magnet ("exit transient" effect) was modeled in ELEGANT according to Ref. [34]. Finally, the effect of radiation shielding [35–37] is neglected, since the wavelength at which CSR starts being suppressed by the vacuum

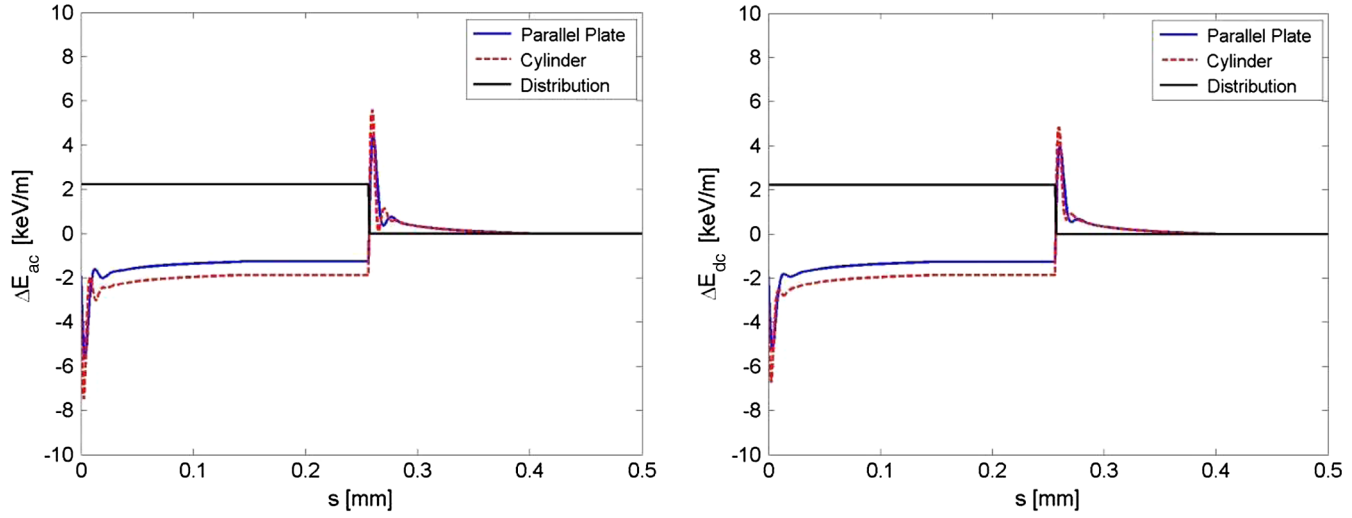

FIG. 4. Single bunch energy variation induced by ac (left) and dc (right) resistive wall impedance excited by a 0.7 nC, 0.8-ps-long uniform charge distribution (black line) in a parallel plate (solid line) and cylindrical (dashed line) aluminum vacuum chamber. The inner radius of the cylinder is 3.5 mm and equal to the vertical half gap of the parallel plate.

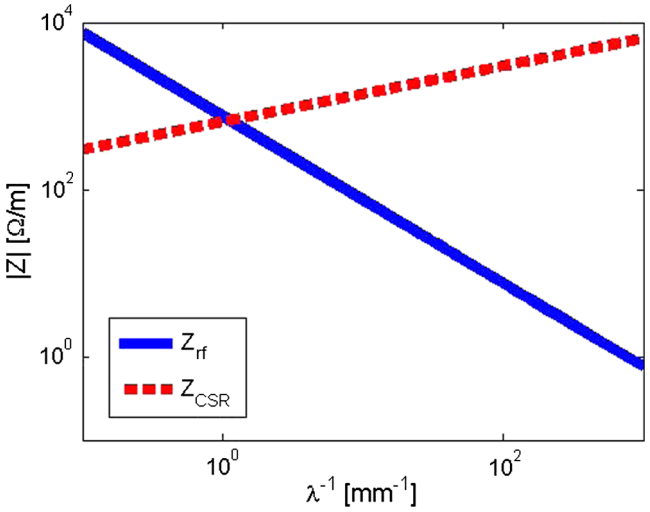

FIG. 5. Spectral behavior of the rf geometric [Eq. (3)] and CSR impedance [Eq. (9)] per unit length. Z_{rf} is calculated for an iris radius of 5 mm (average value in the FERMI BTW structures), and Z_{CSR} is calculated for a curvature radius of 4 m (typical of FERMI BC1).

chamber, $\lambda \geq 2h\sqrt{h/R} \geq 1$ mm (h is the vacuum chamber gap and R the bending radius), is much longer than the electron bunch length under consideration, 10 μm $\leq \sigma_z \leq$ 150 μm. In the FERMI BC1, most of the CSR physics is described by the steady-state emission [18,20], which is represented by the impedance per unit length [24]:

$$Z_{\mathrm{CSR}}(k) = \frac{Z_0 k^{1/3}}{\pi R^{2/3}}(0.41 + \mathrm{i}0.23). \tag{9}$$

The 1D approximation is expected to fail for bunches approaching full compression, i.e., upright longitudinal phase space. In this case, CSR direct transverse forces and the dependence of the longitudinal electric field on the transverse coordinates become important. Since ELEGANT projects the charge distribution onto a line charge, an artificially stronger CSR interaction is expected to be simulated, whereas the actual interaction is somehow "diluted" in the transverse plane [20].

Figure 5 compares the spectral behavior of the geometric rf [Eq. (3)] and steady-state CSR impedance per unit length [Eq. (9)]. They are evaluated for a linac iris radius and dipole curvature radius typical at FERMI. The stronger CSR effect happens in the fourth dipole of BC1, where the bunch is shortened to its minimum rms length of approximately 75 μm. At such a (inverse) length, Z_{CSR} is ~10 times larger than Z_{rf}. Nevertheless, the effect on the particles' longitudinal momentum must be evaluated by integrating Z_{CSR} over the dipole length of ~0.4 m and Z_{rf} over the linac length of tens of meters. The overall machine impedance is therefore expected to be dominated by the contribution of the rf structures.

III. SIMULATION AND EXPERIMENT RESULTS

A. Linac

The effect of wakefields on the particle dynamics in FERMI was simulated with ELEGANT. The code convolutes the charge distribution produced by tracking with geometric wake functions provided as external text files. CSR is simulated in the 1D approximation, including entrance and exit transient effects. The quantities in Eq. (2) predicted by the code at the linac end were compared with the corresponding measured quantities. Table I summarizes the main linac and electron beam parameters adopted in the experiment and used in the simulations.

In the experimental setup, a dipole magnet installed at the linac end bends the beam horizontally and sends it to a screen with a nonzero energy-dispersion function. The beam is matched to optics functions that make the geometric beam size at the screen negligible with respect to the chromatic beam size, i.e., $\sqrt{\varepsilon_x \beta_x} \ll \eta_x \sigma_\delta$. Thus, the horizontal particle coordinate at the screen is proportional to its energy deviation times the dispersion function. The error bar applied to the measured values of beam mean energy (~0.1%) and energy spread (~1 MeV) is mostly contributed, for a given dipole field calibration and theoretical dispersion function, by trajectory misalignment, which is in turn associated to a spurious dispersion function. The reproducibility of the measurements over consecutive shots is within the aforementioned uncertainties.

However, the *absolute* value of the beam mean energy and energy spread is affected by the uncertainty on the actual rf peak voltages and phases, dipole field calibration, dispersion function, and screen alignment. As a matter of fact, the beam longitudinal phase space at the linac end was measured [38] for the bunch charge of 0.7 nC and for the

TABLE I. FERMI electron beam and linac parameters for the nominal bunch length compression factor. Asterisks mark simulated-only parameters. 0.7 nC bunch charge is the nominal working point of FERMI. The bunch charge of 0.35 nC was obtained by lowering the gun photoinjector laser pulse energy.

Parameter	Value	Units
Charge	0.35, 0.70	nC
Peak current at injector exit	35*, 70*	A
Linac-1 rf phase	116.5	deg
Energy at BC1	0.28	GeV
BC1 dipole bending angle	85	mrad
BC1 compression factor	10*, 11	
Final peak current (bunch core)	400*, 750	A
Final bunch Duration, FWHM	0.3*, 0.8	ps
Energy spread at linac end, rms	1.2, 1.9	MeV
Mean energy at linac end	1.451, 1.445	GeV

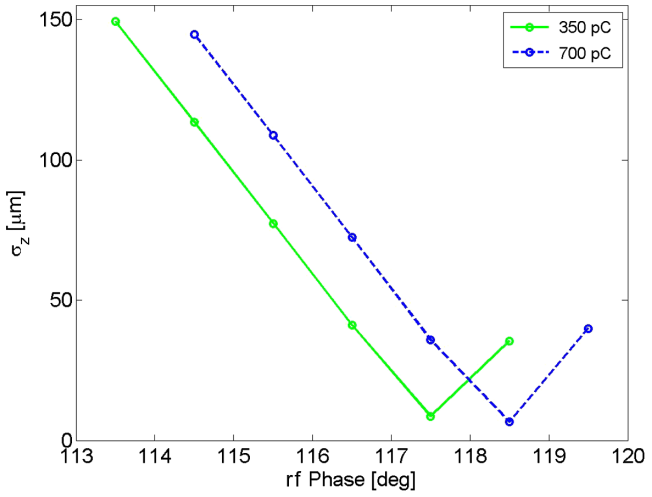

FIG. 6. Simulated rms bunch length at the linac end as function of the $L1$ rf phase.

nominal compression factor (see Table 1). For such a specific setting *only*, three parameters were modified in the simulation to match the measured mean energy and energy spread: (i) the peak voltage of the X-band structure was lowered by 2 MV over the nominal setting of 22 MV; (ii) the peak voltage of one BTW structure in $L4$ was increased by 2 MV over the nominal value of 142 MV; (iii) the rf phase of the last BTW structure in $L4$ was shifted by a 2 deg S band. After this tuning of the simulation setup, the rf phase of $L1$ was varied in the code in order to scan the final bunch length, as shown in Fig. 6. Finally, the mean energy and energy spread predicted by the code were compared with measured quantities, as illustrated in Figs. 7 and 8. The comparison was repeated at the bunch charge of 0.35 and 0.70 nC.

Figures 7 and 8 suggest that the 1D CSR modeling in ELEGANT overestimates the strength of the interaction at full compression (this is defined by the rf phase for minimum bunch length in Fig. 6): In Figs. 7(a) and 8(a), the simulated mean energy is 2–3 MeV lower than the measured one; i.e., CSR is predicted to induce a higher beam energy loss than in reality. At the phase of full compression we also observe, in Figs. 7(b) and 8(b), the largest discrepancy in the beam energy spread; i.e., CSR is predicted to induce a larger energy spread than in reality. Instead, an excellent agreement is obtained both in mean energy and energy spread for all other rf phases. In addition to this, Figs. 7 and 8 confirm that, as discussed already in Sec. II D, the longitudinal effect of CSR is negligible with respect to the linac geometric impedance for bunch lengths longer than ~50 μm.

The successful benchmarking of simulation and experiment results for rf phases far from the point of full compression confirms the reliability of the model adopted for the linac geometric wakefields. Moreover, one is allowed to infer that the linac geometric wakefields dominate the beam dynamics over other collective effects not considered here, such as space charge forces in the main linac, geometric wakefields associated to discontinuities of the beam pipe outside the accelerating structures, and linac resistive wall wakefield.

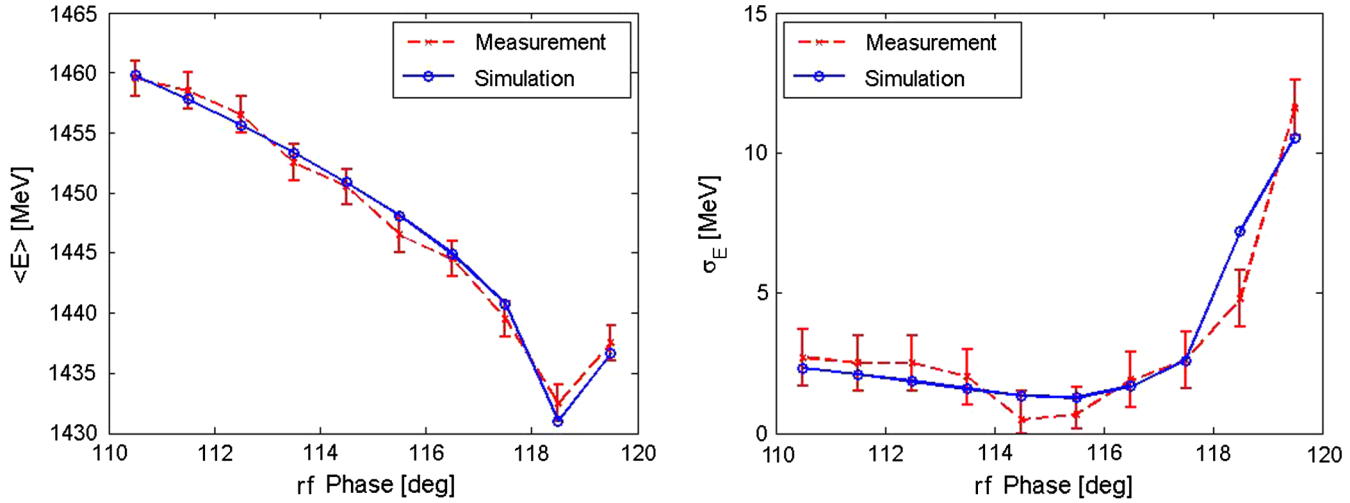

FIG. 7. Simulated and measured beam mean energy (left) and rms energy spread (right) at the linac end as a function of the $L1$ rf phase, for 0.7 nC bunch charge. In both plots the largest discrepancy between experiment and simulation is in the correspondence of 118.5 deg rf phase, i.e., at the point of full compression (see Fig. 6). The left plot suggests that the 1D CSR modeling in ELEGANT overestimates the strength of the interaction at full compression (compare the red dashed line with the solid blue line). In the right plot, the large discrepancy at the phase of full compression is due to the discrepancy in the energy spread induced by CSR, which sums to that one determined by rf curvature and longitudinal geometric wakefields. Each measured data point is the average of ten consecutive measurements.

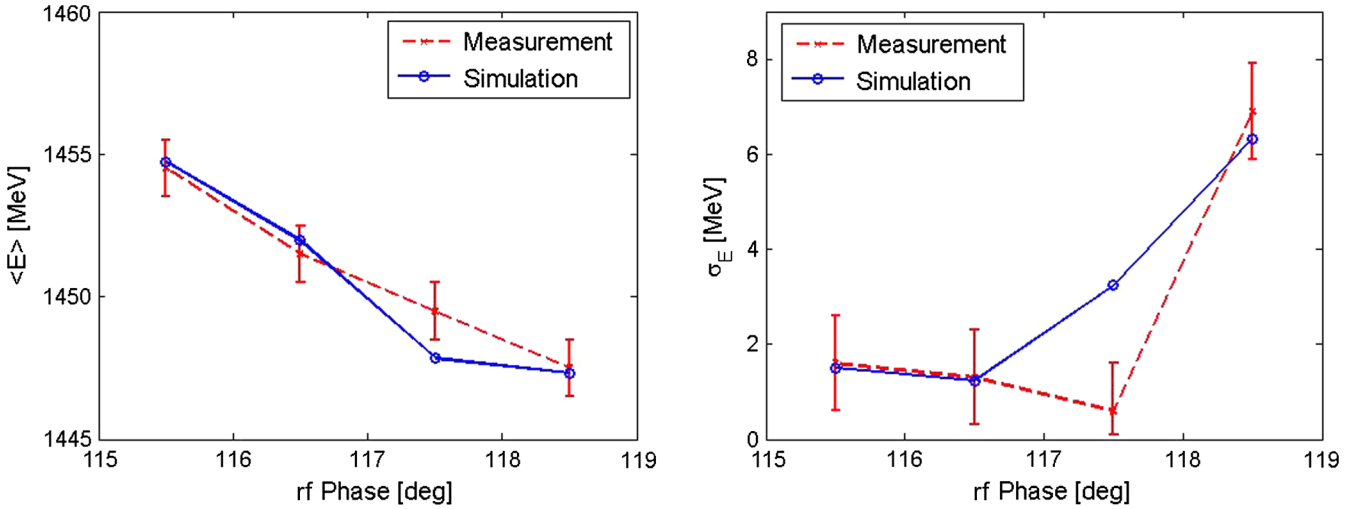

FIG. 8. Simulated and measured beam mean energy (left) and rms energy spread (right) at the linac end as a function of the $L1$ rf phase, for 0.35 nC bunch charge. In both plots the largest discrepancy between experiment and simulation is in the correspondence of 117.5 deg rf phase, i.e., at the point of full compression (see Fig. 6). The left plot suggests that the 1D CSR modeling in ELEGANT overestimates the strength of the interaction for full compression (compare the red dashed line with the solid blue line). In the right plot, the discrepancy at the phase of full compression is due to the discrepancy in the energy spread induced by CSR, which sums to that one determined by the rf curvature and longitudinal geometric wakefields. Each measured data point is the average of ten consecutive measurements.

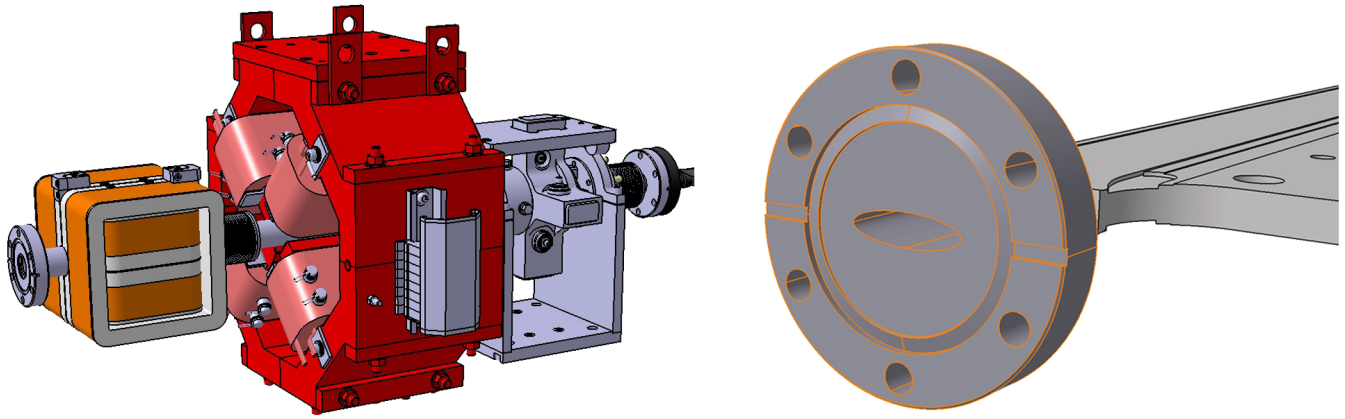

FIG. 9. 3D rendering of the cylindrical stainless steel 304LN, 1.1-m-long vacuum chamber of the interundulator section (left) and of the elliptical aluminum 3.2-m-long undulator vacuum chamber (right). The inner chamber dimensions are, respectively, 22 mm diameter and 7 mm × 22 mm inner diameter. The cylindrical pipe is surrounded by steering coils, a quadrupole magnet, and a cavity beam position monitor.

B. Undulator

The FERMI FEL-2 undulator vacuum chamber is made of aluminum elliptical sections, surrounded by undulators, alternated with stainless steel cylindrical sections, surrounded by other magnetic and diagnostic elements, as shown in Fig. 9 (see also Sec. II C). The longitudinal resistive wall wake function was calculated as the inverse-Fourier transform of Eq. (5) for the cylindrical sections and of Eq. (7) for the elliptical sections. Figure 10 compares the simulated electron beam longitudinal phase space at the end of the undulator line, with and without resistive wall wakefields. Particle tracking reveals that only a ∼100-fs-long portion of the bunch head is affected by resistive wall wakefields; even in that region, the energy spread is weakly affected, at the level of 0.1%. Owing to the fact that the vacuum ultraviolet seed laser that initiates the FEL process at FERMI is typically ∼70 fs long or shorter [6,7] and that it is superimposed to the central portion of the bunch and with relative arrival time jitter smaller than 50 fs, we can reasonably conclude that the resistive wall wakefield is predicted to have no impact on the lasing efficiency.

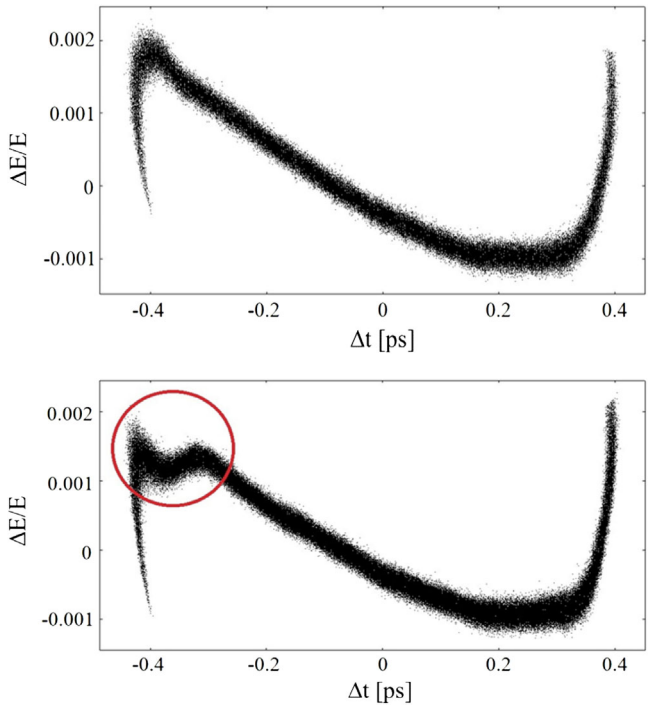

FIG. 10. Simulated longitudinal phase space at the end of the FERMI FEL-2 undulator line, without (top) and with (bottom) resistive wall wakefields. The red circle highlights the region of the bunch head in which wakefields have the most effect. The simulated phase space (top plot) basically illustrates the beam longitudinal phase space at the linac end (no further modification to it is predicted by tracking during the transport from the linac end to the undulator); it matches the phase space measured at the linac end for the nominal FERMI configuration, whose key parameters are summarized in Table 1.

IV. CONCLUSIONS

The simulated effect of longitudinal geometric wakefields in accelerating structures and of 1D CSR in the bunch compressor of the FERMI beam delivery system on the electron bunch energy distribution was experimentally benchmarked by varying the bunch length and the bunch charge. The agreement of the beam mean energy and energy spread values at the linac end confirms a reliable modeling of the linac geometric wakefields, with an overall absolute uncertainty of a few MeV (∼0.1% level) both for the induced mean energy loss and rms energy spread. The study confirms that the linac geometric wakefields dominate the longitudinal beam dynamics at the FERMI nominal working point, together with the rf curvature. CSR plays an important role only at rms bunch lengths shorter than 50 μm, whereas nominal bunch durations at FERMI are longer than 70 μm. Particle tracking through the undulator line in the presence of resistive wall wakefields confirms the limited impact of that impedance on the beam quality and thus on the lasing process. This work complements past studies on the FERMI impedance budget, which were focused on the effect of longitudinal wakefields in the presence of current shaping and of transverse wakefields and CSR on the beam projected emittance. It confirms an overall good understanding of collective effects in the facility.

ACKNOWLEDGMENTS

The authors acknowledge P. Craievich for helpful insights about wakefield modeling and G. Penco for stimulating discussions.

[1] L.-H. Yu *et al.*, High-gain harmonic-generation free-electron laser, Science **289**, 932(2000).
[2] W. Ackermann *et al.*, Operation of a free-electron laser from the extreme ultraviolet to the water window, Nat. Photonics **1**, 336 (2007).
[3] P. Emma *et al.*, First lasing and operation of an ångstrom-wavelength free-electron laser, Nat. Photonics **4**, 641 (2010).
[4] T. Ishikawa *et al.*, A compact X-ray free-electron laser emitting in the sub-ångström region, Nat. Photonics **6**, 540 (2012).
[5] J. Amann *et al.*, Demonstration of self-seeding in a hard-X-ray free-electron laser, Nat. Photonics **6**, 693 (2012).
[6] E. Allaria *et al.*, Highly coherent and stable pulses from the FERMI seeded free-electron laser in the extreme ultraviolet, Nat. Photonics **6**, 699 (2012).
[7] E. Allaria *et al.*, Two-stage seeded soft-X-ray free-electron laser, Nat. Photonics **7**, 913 (2013).
[8] S. Di Mitri and M. Cornacchia, Electron beam brightness in linac drivers for free-electron-lasers, Phys. Rep. **539**, 1 (2014).
[9] S. Di Mitri, Maximum brightness of linac-driven electron beams in the presence of collective effects, Phys. Rev. ST Accel. Beams **16**, 050701 (2013).
[10] P. Craievich, T. Weiland, and I. Zagorodnov, The short-range wakefields in the BTW accelerating structure of the ELETTRA LINAC, Nucl. Instrum. Methods Phys. Res., Sect. A **558**, 58 (2006).
[11] P. Craievich, S. Di Mitri, and A. A. Zholents, Single-bunch emittance preservation in the presence of trajectory jitter for FERMI@elettra-seeded FEL, Nucl. Instrum. Methods Phys. Res., Sect. A **604**, 457 (2009).
[12] P. Craievich, Short-range longitudinal and transverse wakefield effects in FERMI@Elettra FEL project, Ph.D. thesis, Technische Universiteit Eindhoven, Department of Applied Physics, Eindhoven, Netherlands, ISBN 978-90-386-2294-1, 2010.
[13] S. Di Mitri *et al.*, Design and simulation challenges for FERMI@elettra, Nucl. Instrum. Methods Phys. Res., Sect. A **608**, 19 (2009).
[14] S. Di Mitri, Machine design, and electron beam control of a single-pass linac for free electron Laser: The FERMI@Elettra case study, Ph.D. thesis, University of Gronigen, Zernike Institute for Advanced Materials, ISBN: 978-90-367-5176-6, 2011.
[15] M. Cornacchia, S. Di Mitri, G. Penco, and A. A. Zholents, Formation of electron bunches for harmonic cascade x-ray

free electron lasers, Phys. Rev. ST Accel. Beams **9**, 120701 (2006).

[16] G. Penco, M. Danailov, A. Demidovich, E. Allaria, G. De Ninno, S. Di Mitri, W. M. Fawley, E. Ferrari, L. Giannessi, and M. Trovo', Experimental Demonstration of Electron Longitudinal-Phase-Space Linearization by Shaping the Photoinjector Laser Pulse, Phys. Rev. Lett. **112**, 044801 (2014).

[17] S. Di Mitri, L. Froehlich, and E. Karantzoulis, Influence of longitudinally tapered collimators on a high brightness electron beam, Phys. Rev. ST Accel. Beams **15**, 061001 (2012).

[18] S. Di Mitri, E. M. Allaria, P. Craievich, W. Fwaley, L. Giannessi, A. Lutman, G. Penco, S. Spampinati, and M. Trovo', Transverse emittance preservation during bunch compression in the Fermi free electron laser, Phys. Rev. ST Accel. Beams **15**, 020701 (2012).

[19] S. Di Mitri, M. Cornacchia, and S. Spampinati, Cancellation of Coherent Synchrotron Radiation Kicks with Optics Balance, Phys. Rev. Lett. **110**, 014801 (2013).

[20] A. Brynes *et al.*, Beyond the limits of 1D coherent synchrotron radiation, New J. Phys. **20**, 073035 (2018).

[21] P. Craievich, A. Lutman, and R. Vescovo, Electromagnetic field and short-range wake function in a beam pipe of elliptical cross section, Phys. Rev. ST Accel. Beams **11**, 074401 (2008).

[22] A. W. Chao, *The Physics of Collective Beam Instabilities in High Energy Accelerators* (Wiley, New York, 1993).

[23] B. W. Zotter and S. A. Kheifets, *Impedances and Wakes in High-Energy Particle Accelerators* (World Scientific, Singapore, 1998).

[24] J. B. Murphy, S. Krinsky, and R. L. Gluckstern, Longitudinal wakefield for synchrotron radiation, in *Proceedings of the IEEE Particle Accelerator Conference, Dallas* (IEEE, Piscataway, 1996).

[25] Ya. S. Derbenev, J. Rossbach, E. L. Saldin, and V. D. Shiltsev, Microbunch radiative tail–head interaction, DESY Report No. TESLA-FEL 95-05, 1995.

[26] K. L. F. Bane, Wakefields of sub-picosecond electron bunches, Int. J. Mod. Phys. A **22**, 3736 (2007).

[27] N. Ashcroft and N. Mermin, *Solid State Physics* (Harcourt Brace, Orlando, 1976).

[28] K. L. F. Bane and G. Stupakov, Resistive wall wakefield in the LCLS undulator, in *Proceedings of the 21st Particle Accelerator Conference, Knoxville, TN, 2005* (IEEE, Piscataway, 2005), p. 3391.

[29] H. Henke and O. Napoly, Wake fields between two parallel resistive plates, in *Proceedings of the 2nd European Particle Accelerator Conference, Nice, France, 1990* (Editions Frontieres, Nice, France, 1990), p. 1046, ISBN 13 978-2863320907.

[30] H. Wiedemann, *Particle Accelerator Physics*, 2nd ed. (Springer-Verlag, Berlin, 2003), Vol. I, pp. 311–317, ISBN: 3-540-00672-9.

[31] E. L. Saldin, E. A. Schneidmiller, and M. V. Yurkov, On the coherent radiation of an electron bunch moving in an arc of a circle, Nucl. Instrum. Methods Phys. Res., Sect. A **398**, 373 (1997).

[32] M. Borland, ELEGANT: A flexible SDDS-compliant code for accelerator simulation, APS Technical Note No. LS-207, 2000.

[33] M. Borland, Simple method for particle tracking with coherent synchrotron radiation, Phys. Rev. ST Accel. Beams **4**, 070701 (2001).

[34] P. Emma and G. Stupakov, CSR wake for a short magnet in ultrarelativistic limit, in *Proceedings of the 8th European Particle Accelerator Conference, Paris, 2002* (EPS-IGA and CERN, Geneva, 2002), WEPRI029, p. 1479.

[35] J. S. Nodvick and D. Saxon, Suppression of coherent radiation by electrons in a synchrotron, Phys. Rev. **96**, 180 (1954).

[36] R. L. Warnock, Shielded coherent synchrotron radiation and its effect on very short bunches, Stanford Linear Accelerator Center, Stanford University, Report No. SLAC-PUB-5375, 1990.

[37] G. V. Stupakov and I. A. Kotelnikov, Shielding and synchrotron radiation in toroidal waveguide, Phys. Rev. ST Accel. Beams **6**, 034401 (2003).

[38] P. Craievich *et al.*, Implementation of radio-frequency deflecting devices for comprehensive high-energy electron beam diagnosis, IEEE Trans. Nucl. Sci. **62**, 210 (2015).